Characterization of breast tomosynthesis systems: A comparison and optimization

Thanh Tra Pham

Supervision

Anders Tingberg, Magnus Dustler and Pontus Timberg

This work has been conducted at
Medical Radiation Physics, Skane University Hospital, Malmö

Department of Medical Radiation Physics,
Clinical Sciences, Lund
Lund University

Contents

Abbreviations

2D – two-dimensional

3D – three-dimensional

AEC – Automatic exposure control

AGD – Average glandular dose

ASF – Artifact spread function

BT – Breast tomosynthesis

CC – Craniocaudal

CT – Computed tomography

DM – Digital mammography

FBP – Filtered back projection

FWHM – Full-width-at-half-maximum

IR – Iterative reconstruction

MLO – Mediolateral oblique

PSF – Point-spread-function

ROI – Region of interest

SDNR – Signal-difference-to-noise ratio

SNR – Signal-to-noise ratio

Abstract

Aim: The aim of the study is to characterize the dependency of image quality on absorbed dose for two breast tomosynthesis (BT) systems, GE Senographe Pristina and Siemens Mammomat Inspiration and compare the systems. The image quality was evaluated by different parameters such as: in-plane and in-depth spatial resolution, artifact spread function (ASF) and signal-difference-to-noise ratio (SDNR).

Material & Method: In this work, BT volumes were acquired using one GE and one Siemens system with different acquisition and reconstruction settings. For the Siemens system, two reconstruction algorithms were evaluated, one is used in our clinic Unilabs Skåne, and the other is a newly developed reconstruction algorithm called *EMPIRE*. For the GE system, the algorithm used in clinical routine was evaluated. The phantoms used were CIRS phantoms with and without anatomical background (models 020 and 021), including imaging targets simulating microcalcifications and carcinomas. The thickness of these phantoms could be varied to simulate different breast thicknesses. Another in-house made phantom was used for measurement of the depth resolution. The image quality was evaluated on reconstructed images.

Result: For all breast thicknesses, the GE system used a lower automatic exposure control (AEC) dose in comparison with the Siemens system. At AEC settings, the in-plane resolution of the two systems are comparable, although GE has slightly smaller FWHM compared with Siemens (330 µm vs. 380 µm in the tube motion direction, 290 µm vs. 340 µm in the orthogonal direction). Regarding the depth resolution, the FWHM of the GE system is higher than that of the Siemens system (2.3 mm vs 5.5 mm). Also, GE has narrower ASF for microcalcifications compared with Siemens (3.1 mm vs 5.0 mm). For the larger objects simulating carcinoma, however, Siemens has narrower ASF compared with GE (9.8 mm vs 13.9 mm).

For all breast thickness, the GE system provides the same SDNR value at lower dose than the Siemens system with the reconstruction algorithms currently in use. However, with the newly developed algorithm *EMPIRE*, the SDNR value is generally higher than Siemens *TOMO_STANDARD* and comparable or higher than GE. With consideration to the anatomical noise, a dose increase does not result in a significant SDNR gain.

Conclusion: In this study, there is no clear advantage of any system. Both systems have good performance in different aspects and there are some uncertainties that need to be considered.

Regarding the optimization, the results did not motivate a dose increase for SDNR gain.

The studied parameters may not be representative for the image quality desired by radiologists and thus, further qualitative study is necessary.

Summary in Swedish (Populärvetenskaplig sammanfattning)

Kan man förbättra metoden för att upptäcka bröstcancer?

Bröstcancer är den vanligaste cancertypen bland kvinnor och varje år drabbas nästan 9000 kvinnor i Sverige. Vart tredje cancerfall hos kvinnor är bröstcancer. De flesta fall upptäcks via screeningprogrammet där en så kallad mammografiundersökning ingår. Alla kvinnor mellan 40 och 74 år är inbjudna till denna undersökning.

Mammografi är en röntgenundersökning av bröst. Under röntgenbildtagningen får bröstet ligga mot en platta medan en annan platta trycker mot bröstet för att jämna ut bröstvävnaden. Bröstet har tre dimensioner medan bilden har bara två, och därför händer det ibland att bröstvävnad överlappar och kan se ut som en tumör. Det kan också hända att en riktig tumör gömmer sig bakom frisk vävnad. För att lösa dessa problem kan man utnyttja en teknik som kallas för brösttomosyntes som kan användas som ersättning eller som komplement till vanlig mammografi. Bildtagning med brösttomosyntes går till på samma sätt som i mammografi, men röntgenröret rör sig längs en båge över bröstet istället för att vara stilla och bildtagningen sker från flera vinklar. Med hjälp av dessa bilder skapas en avbildning av bröstet i 3D. På detta sätt kan man studera bröstet vid olika djup och undvika överlappningen av vävnad som kan uppkomma i en mammografibild.

Det finns flera brösttomosyntesmaskiner av olika design och teknik ute på marknaden. I detta arbete ville jag utvärdera 3D-bilder från maskiner från två olika tillverkare, Siemens Healthineers och GE Healthcare. Jag mätte bildernas kvalitet och mängden stråldos som krävdes för en viss bildkvalitetsnivå. Mätningen gjordes med hjälp av olika bröstfantom, det vill säga modeller med bröstliknande material. I fantomen fanns även tumör- och kalkliknande strukturer som jag kunde använda i min utvärdering.

Resultaten visar att maskinerna är relativt lika i detaljupplösning i alla tre dimensioner. För båda maskinerna kan man öka stråldosen och få lite bättre kontrast hos tumörerna. Det är dock inte motiverat att öka dosen för en så liten förbättring i kontrast. Dessutom var dosen för Siemensmaskinen redan nära den europeiska dosgränsen så en ökning var inte aktuell. Däremot har Siemens en nyutvecklad mjukvara för att skapa 3D bilden, och med den förbättras kontrasten avsevärt. För GE-maskinen är dosen väsentligt lägre än den europeiska dosgränsen, och i detta fall är det möjligt att öka stråldosen. Kontrasten är däremot inte allt som behövs för att upptäcka cancer och det behövs fler mätningar med avseende på andra aspekter för att dra en slutsats kring detta.

Resultaten från denna studie kan inte fullt representera hur radiologer upplever bilderna. Det skulle därför vara värdefullt att få radiologers bedömning på både fantombilder och patientbilder.

1   Introduction

Breast cancer is the most frequently diagnosed cancer among women in Sweden with 8923 cases diagnosed in 2016 (1). A Swedish breast cancer screening program is established for early detection which is estimated to reduce the mortality rate by 16-25% (2). Women between 40 and 74 years of age are invited to the breast examination which comprises digital mammography (DM), an X-ray based imaging method resulting in two-dimensional (2D) images. An important limitation of the method is the overlap of anatomical structures, which may cause normal breast tissue to hide true lesions (false negative) or to appear like true lesions (false positive) (3). A solution to the problem is breast tomosynthesis (BT), a limited-angle tomographic technique enabling three-dimensional (3D) imaging. Multiple low-dose projection images are acquired over a limited angular range and subsequently used to reconstruct the breast volume in slices parallel to the detector surface (4).

The benefits of using BT in the screening program has been reported by different studies. The use of BT in addition to standard DM in screening program improves breast cancer detection and may reduce the false positive recalls, concluded in a large scale study by Ciatto et al.(5). Another population-based study by Zackrisson et al. (6) even suggests that one view-BT as a stand-alone screening modality increases the cancer detection rate in comparison to the standard two views-DM.

1.1   Aim

Manufacturers take different implementations to the BT technique, as there are variations in parameters such as angular range, number of projections, dose distributions, X-ray tube motion and reconstruction algorithm (3). In Skåne Unilabs, there are two different BT systems, GE Healthcare Senographe Pristina and Siemens Mammomat Inspiration Tomo. There have been mixed perceptions from the radiologists regarding the newer GE system, but there are no studies that directly compare the two, distinctly different, systems. Thus, the aim of this work was to:

1. Characterize and compare the image quality of the reconstructed data and absorbed dose of the systems. The image quality was evaluated by the following parameters: spatial resolution (both in plane and depth), artifact spread function (ASF) and signal-difference-to-noise ratio (SDNR).
2. Analyze the relation between SDNR and average glandular dose (AGD) for optimization of both systems.

2 Background

2.1 Mammography

The current standard imaging method in breast screening is two-view DM, in bilateral craniocaudal (CC) and mediolateral oblique (MLO) views. The imaging method was implemented from the mid and late 1920s to examine patients with palpable breast abnormalities. The technique has since been developed and improved to be more extensively applicable in the clinic (7).

In the early 1960s, the X-ray source of the mammography system generally consisted of a tube with a tungsten anode, modified to allow for lower kilovoltage than the conventional X-ray systems at the time. Little to no compression was applied to the breast during the image acquisition. Also, due to the slow recording systems which caused high absorbed dose, a grid or other anti-scatter methods were generally not used (7, 8).

In the next decade, better exposure geometry and lower radiation dose was achieved as more dose efficient recording systems such as screen-film systems were developed. In screen-film system, the screen-phosphor absorbs X-rays much more efficient than the direct film, thus needing fewer incident X-rays for imaging (7). Another major advancement in mammography was the use of molybdenum anodes instead of tungsten (9). At the same kilovoltage, the molybdenum anode delivered a photon spectrum with a lower mean energy than tungsten, thus optimizing the image contrast. By using a grid, the image contrast is further enhanced as the amount of scattered radiation reaching the screen-film is reduced. Most systems included a compression part, contrary to earlier systems (10).

Today, DM is the standard method for breast imaging. It is a major improvement from film-screen technology in terms of both image quality and radiation dose. Generally, the radiation dose can be reduced significantly by reducing the tube loading while increasing the tube voltage. Thus, molybdenum with a soft beam spectrum is not as preferable as tungsten. Also, as digital detector has a larger dynamic range than screen-film, it can exploit harder spectrums and enables the use of tungsten target in modern systems (11). One another significant property of DM which differs from film-mammography is that the processes of image acquisition, storage and display are decoupled, allowing separate optimization in each step. Another benefit with DM is

that digital image management and processing allows quantitative imaging techniques such as breast tomosynthesis (12).

2.2   Breast tomosynthesis

Digital X-ray tomosynthesis is an improvement of conventional geometric tomography. In conventional geometric tomography, the X-ray tube and the detector move simultaneously on opposite sides of the patient, producing in-focus images of the plane of interest that includes the pivot point of the machine (Figure 1). The limitation of the technique is that only a single focus plane can be acquired from one acquisition sequence (13).
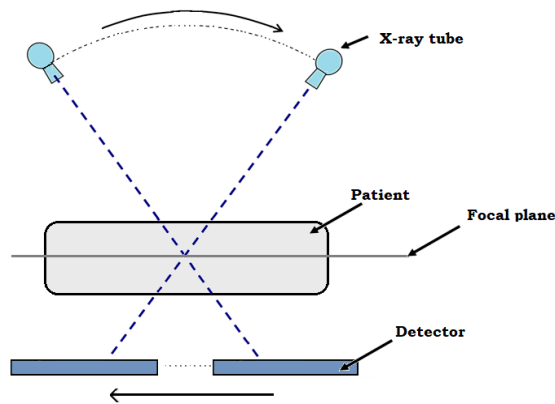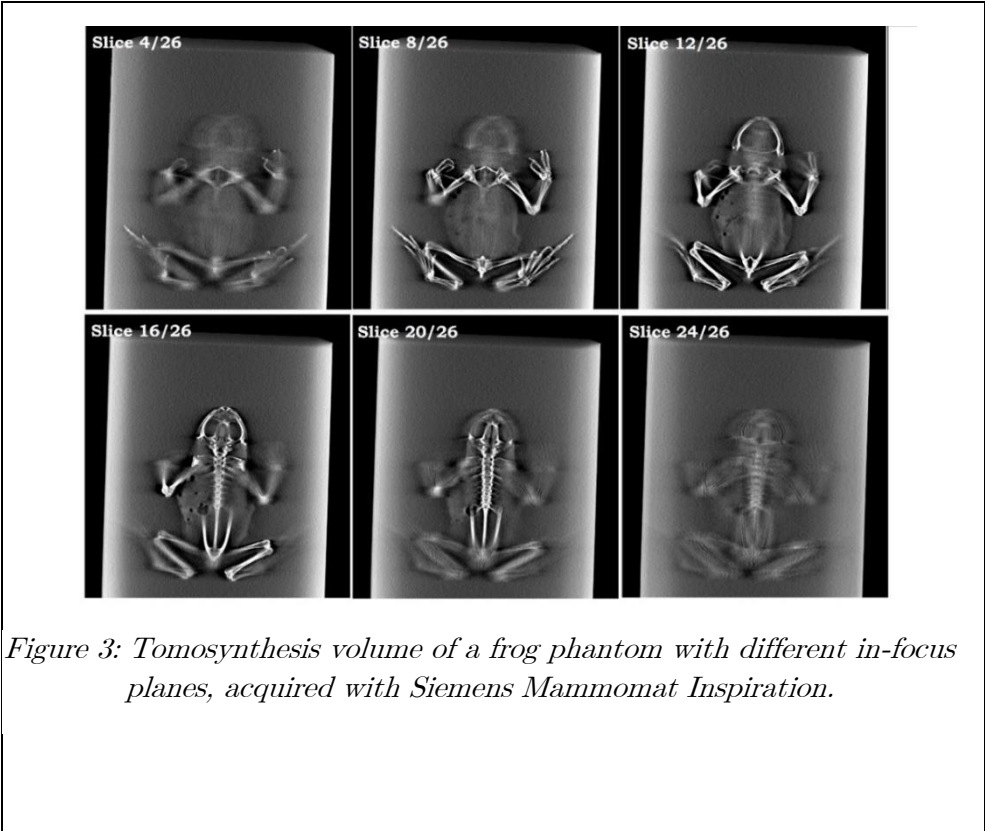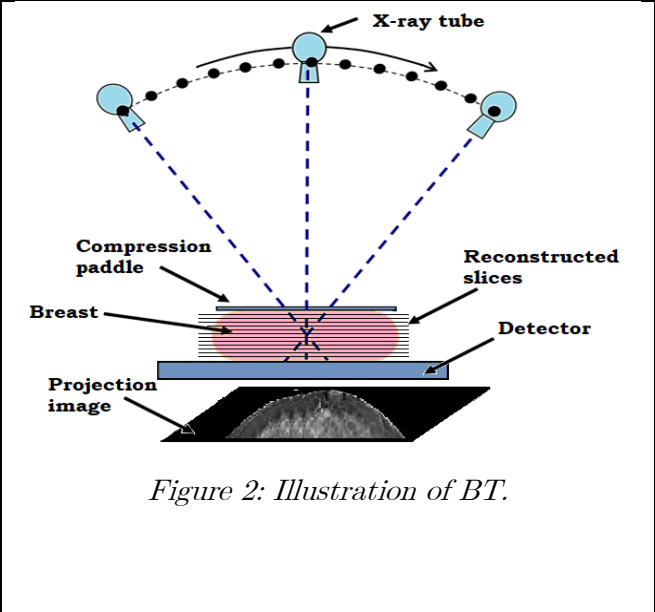

Figure 1: Illustration of conventional geometric tomography.

Tomosynthesis, contrary to conventional geometric tomography, generates several in-focus planes at different depths from a single acquisition sequence. The in-focus planes are created by shifting and adding the projection images, and the depth at which the structures are in-focus is determined by varying the amount of shifting. This method is mathematically equivalent to unfiltered back projection and is not in practical use. Instead, other 3D reconstruction methods such as filtered back projection (FBP) are developed. Unlike computed tomography (CT), tomosynthesis uses a limited angular range and the reconstruction is performed on incomplete data sampling, resulting in residual blur from objects outside the focus plane. Since the introduction of flat panel detectors with large area and rapid read-out, tomosynthesis has become clinically applicable in many fields, including mammography (13).

The use of tomosynthesis in breast imaging was first demonstrated by Niklason et al. in 1997 where BT was implemented in a modified mammography device (4). In BT, the compressed breast and the detector remain stationary while the X-ray tube travels along an arc over the breast, acquiring a number of low dose projection images. The

total dose for one tomosynthesis acquisition is typically between one and two times the dose of the corresponding DM projection (Figure 2). The projection images are subsequently reconstructed into a 3D volume of in-focus slices parallel to the detector plane (Figure 3) (4).

Figure 2: Illustration of BT.

Figure 3: Tomosynthesis volume of a frog phantom with different in-focus planes, acquired with Siemens Mammomat Inspiration.

2.3   Factors affecting image quality and radiation dose

The image quality of a BT volume and the patient radiation dose are dependent upon several factors, some of which are the fundamental design and technology of the system, while some others are acquisition parameters that the operator can manipulate for optimal results. In this section, an overview of some factors influencing image quality and radiation dose are presented.

2.3.1   Tube loading

Tube loading is the product of the tube current and the exposure time, affecting both image quality and patient radiation dose. The tube loading is generally determined using automatic exposure control (AEC) to keep the dose to the detector constant.

The relationship between tube loading and absorbed dose is proportional, meaning a 50% decrease in tube loading will result in 50% decrease in absorbed dose. However, a low tube loading also affects the image quality negatively as a lower number of emitted photons increases the quantum noise and decreases SDNR (12).

2.3.2   Tube voltage and beam quality

Due to the small difference in attenuation coefficients of the breast tissues, the beam quality in mammography is different from general radiography. The X-ray energy in mammography is significantly lower than in general radiography to achieve reasonable contrast (14).

The beam quality is determined by the tube voltage settings and anode/filter material. The X-ray spectra for mammography composes of continuous spectrum of bremsstrahlung and peaks of the characteristic X-ray radiation. As the photon fluence at the characteristic energies is high, the anode material must have characteristic energies near the optimum energy for mammography (14). The common anode materials are molybdenum and tungsten. Compared to molybdenum, tungsten provides spectra with higher mean energies and may be more suitable for thick and dense breasts. Some manufacturers use multiple anode/filter combinations that can be selected by the system operator.

The tube voltage settings regulate the maximum energy of the continuous spectrum but also the efficiency of the photon production. Thus, high tube voltage settings are allowed even though high energy photons are undesirable in mammography. These photons are efficiently attenuated by the filter, the material of which determines the k-edge energy where the photon attenuation coefficient abruptly increases. The filter also

prevents low energy photons from reaching the patient, thus further reducing the dose (14).

2.3.3 Detectors

There are two main types of flat-panel detectors, direct and in-direct conversion. For the former type, the photon interacts with the photoconductive layer, for example amorphous selenium (a-Se), creating electrical charges that are directly registered. For the latter type, the detector is scintillator-based, meaning visible light photons are created by the X-ray interactions. These scintillation photons are subsequently converted into electrical charges using photodiodes. A commonly used indirect detector is cesium iodide (Cs-I) (15).

For the indirect conversion detector, the light produced by the scintillator is scattered causing blur, resulting in poor resolution compared to direct conversion detector. To prevent this, the scintillator is built up in a needle structure, similar to light tubes. The indirect conversion detector has high detective quantum efficiency (DQE) at low frequencies. However, as the blurring is dependent on absorption depth, the DQE of indirect conversion detector decreases more rapidly at high frequencies relative to a direct conversion detector. Higher DQE generally allows for higher signal-to-noise ratio (SNR) at a given dose level or reduced patient dose at the same SNR-value (15).

2.3.4 Number of projection views and total angular range

The geometry of the image acquisition has high impact on the image quality. A larger number of projection views should mathematically yield better artifact reduction, which is also proved in various studies (16-20). However, the number of projection views is limited by total exposure for all projection views, and in turn by the patient dose. While maintaining the total exposure and increasing the number of projection views, the exposure per projection view decreases and results in increasing quantum noise in each view. Also, the electronic noise of the detector increases with the number of projections, as it is constant per projection and independent of the exposure per projection view (18).

By maximizing the total angular range, the in-depth resolution and the artifact spread function (ASF), which describes out-of-plane blurring, are improved (18, 20-22). However, the SDNR can be improved by increasing the tube loading per projection and therefore can be better in narrow angular range. The in-plane resolution in the direction of the X-ray source motion is also suggested to be improved by a narrow angular range (21).

2.3.5   Reconstruction algorithm

The simple shift-and-add method is not valid in the reconstruction of BT due to the acquisition geometry (4). Instead, the widely used reconstruction algorithms for BT are filtered back projection (FBP) and iterative reconstruction (IR).

Various studies have focused on comparison between different reconstruction algorithms. Wu et al. (23) compared simple back projection (SBP), FBP and IR using phantom and patient images. IR provided a significantly higher signal-difference-to-noise ratio (SDNR) for masses compared to FBP. For microcalcifications, FBP provided overall better sharpness compared to IR. However, the noise of FBP is higher, thus degrades the sharpness of the microcalcifications with low contrast. Another study by Zhou et al. (18) used simulation to compare FBP with different filters with IR. The results suggested that IR provides higher image quality regarding in-plane resolution, SDNR and ASF. However, FBP can provide the same image quality if increasing the projection views from 11 to 21 views and the total angular range from $\pm15°$ to $\pm30°$.

Although IR reduces artifacts in BT effectively, it comes with the cost of higher computational burden than FBP. Abdurahman et al. (24) attempted to reduce out-of-plane artifacts by implementing a statistical model on FBP. The model, based on regression of training data from real patient cases, can predict the distribution parameters of artifact-free voxels. The authors observed a reduction of out-of-plane artifacts and improvement in the contrast of masses by implementing the model. The algorithm is implemented by Siemens and is called EMPIRE.

3   Material and Methods

3.1   Description of systems

In this study, two BT systems used in clinical practice are evaluated: GE Healthcare Senographe Pristina and Siemens Mammomat Inspiration Tomo. An overview of the technical specifications of the systems is presented in Table 1.

The systems use different beam qualities because of different target/filter combinations. The GE system has two target/filter combinations (Mo/Mo and Rh/Ag) for different breast sizes while for Siemens, only one combination (W/Rh) is used. The X-ray tube motion of the systems also differs, the Siemens system acquires projections with continuous tube motion, whereas the GE system uses step and shoot.

Both systems use full field flat panel detectors with similar size, however the detector in the Siemens system is a direct conversion detector (a-Se) while the GE system has an indirect conversion detector (CsI-Si). The systems also differ in acquisition geometry, as the Siemens system has an angular range of 50° (± 25°) with 25 projections while the GE system has a narrower angular range of 25° (± 12.5°) with 9 projections.

As for the reconstruction, GE uses an iterative reconstruction algorithm while Siemens uses FBP. Additionally, Siemens has a newly developed FBP reconstruction algorithm with iterative optimizations named 'EMPIRE', which is described in section 2.3.5. The algorithm is currently not used in our clinic. For both systems, the reconstructed slice thickness is 1mm.

Table 1: Technical specifications of the BT systems

BT systems		Siemens Mammomat Inspiration	GE Senographe Pristina
X-ray tube	Target/filter combination	W/0.05 mm Rh	Mo/0.03 mm Mo Rh/0.03 mm Ag
	Motion	Continuous	Step and shoot
Detector	Type	a-Se	CsI-Si
	Size [cm]	24 × 30	24 × 29
	Pixel size [µm]	85	100
	Grid	No	Yes
Acquisition	Angular range [deg]	50	25
	Number of projections	25	9
	Scan time [s]	25	7
	Source to detector distance [cm]	65.5	66
	Detector to center of rotation distance [cm]	4.7	4

Reconstruction	Algorithm	FBP FBP with iterative optimizations	Iterative
	Slice thickness [mm]	1	1

3.2 Test equipment

The evaluation of image quality parameters was performed using mainly CIRS Digital Breast Tomosynthesis QC Phantom, model 021 (CIRS, Norfolk, Virginia, USA). The phantom consists of eight semicircular shaped homogenous slabs (110 mm × 180 mm × 5 mm/10 mm) of breast equivalent material with 50/50 ratio of glandular and adipose tissue (BR50/50). All slabs are 10 mm thick except for one that is 5 mm thick. The phantom thickness can be adjusted to a maximum of 75 mm by using different combinations of homogenous slabs (Figure 4). A special slab is also included, with imaging targets such as material simulating spherical masses of breast carcinoma and glass specks simulating calcification clusters (Figure 5).
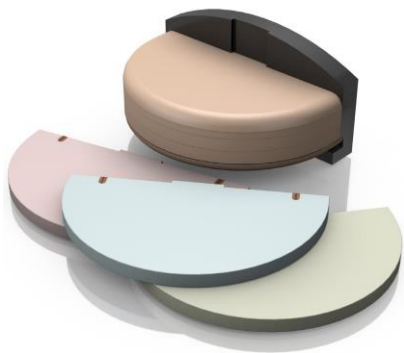

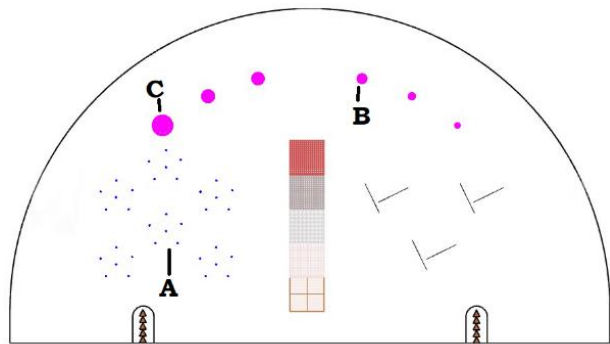Figure 4: CIRS Digital Breast Tomosynthesis QC Phantom, model 021

Figure 5: Homogenous slab with imaging targets (110 mm × 180 mm × 10 mm). A: 330 μm diameter glass specks. B: 6.3 mm diameter spherical mass. C: 3.1 mm diameter spherical mass.

Another CIRS phantom used for the measurement of SDNR is BR3D Breast Imaging Phantom, model 020 (CIRS, Norfolk, Virginia, USA), the so-called "Swirl phantom". The phantom consists of 6 semicircular shaped slabs (110 mm × 180 mm × 10 mm) made of heterogenous breast equivalent material which simulates the anatomical background in the breast. The phantom materials, mimicking 100% adipose and 100% gland tissue, are blended together in a 50/50 ratio to create a swirled pattern in the

phantom (Figure 6). Similar to the previously described phantom, a special slab containing imaging targets simulating spherical masses of breast carcinoma and glass specks simulating calcification clusters is included (Figure 7).

For the measurement of the in-depth resolution, a phantom was made in-house (Figure 8). In the phantom, a metal wire with 150 µm diameter was spanned tilted in air, supported by a 2.8 cm thick PMMA plate. Two broader PMMA plates of 1.9 cm thickness each was placed above and under the supporting plate to provide a background as the reconstruction option *TOMO_STANDARD* of Siemens was unavailable without the background.
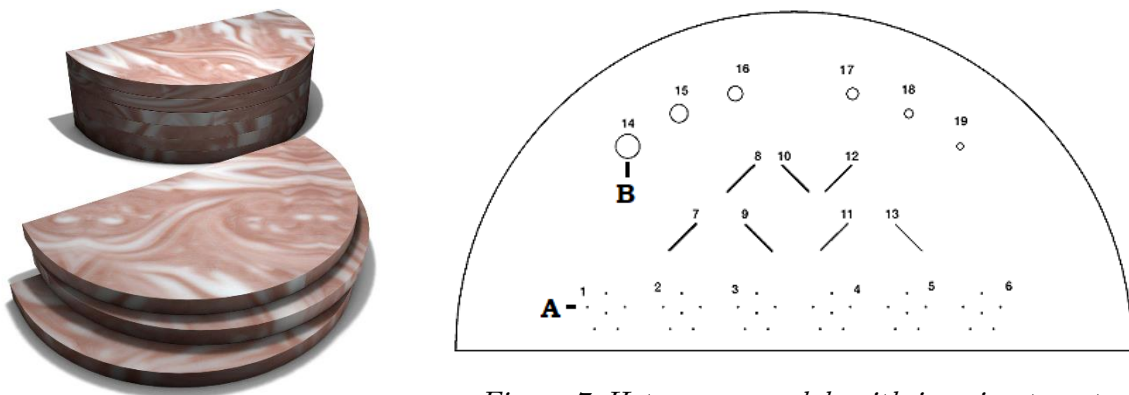

Figure 6: CIRS BR3D Breast Imaging Phantom, model 020

Figure 7: Heterogenous slab with imaging targets (110mm × 180mm × 10mm). A: 400 µm diameter glass specks. B: 6.3 mm diameter spherical mass.
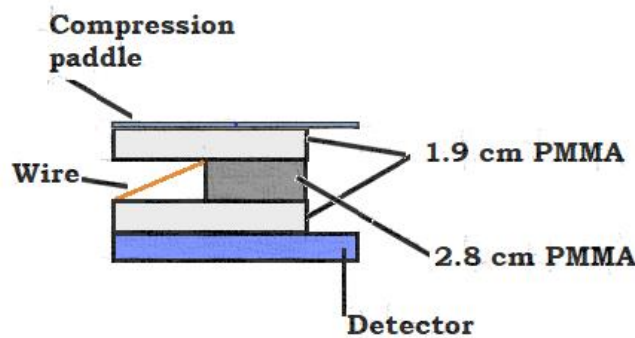

Figure 8: Phantom consisting of supporting PMMA plates and slanted metal wire for the measurement of in-depth resolution.

3.3   Spatial resolution

3.3.1   In-plane resolution

For the measurement of the in-plane resolution, the slab with imaging targets (CIRS model 021, Figure 5) was placed in-between four homogenous slabs, with 20 mm under and 15 mm over the imaging target slab, adding up to a total thickness of 45 mm (Figure 9).
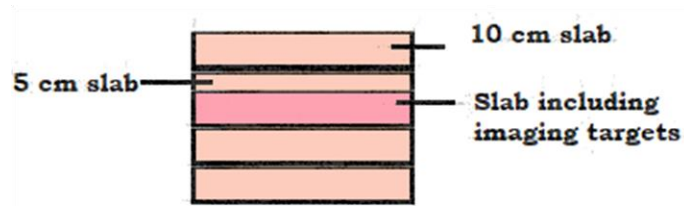

Figure 9: Phantom set up.

The BT image volume was acquired in CC view using AEC settings. As Siemens has multiple AEC options, contrary to GE which only has one option, the *OPDOSE* at normal dose level was selected for exposure. The reconstructions performed were *TOMO_STANDARD* for the Siemens system and the default algorithm *ASiR1* for GE.

The evaluation was based on the glass speck with diameter of 330 µm (Figure 5). As the BT volume was acquired once, the shift variance was not considered. A line profile was made through the center of the speck in the in-focus plane, both parallel (x-direction) and orthogonal (y-direction) to the direction of tube travel. The full-width-at-half-maximum (FWHM) was subsequently determined.

3.3.2   Depth resolution

A reconstructed BT image of the in-house-made phantom (Figure 8) was acquired with the same AEC settings and reconstruction algorithms as described in section 3.3.1. The phantom was aligned so that the wire was orthogonal to the tube travel direction (in *y*-direction).

The tilt angle of the wire, β, was determined as

$$\beta = \arctan\left(\frac{\Delta z}{\Delta y}\right) \qquad (1)$$

where Δz is the distance between the ends of the wire in-depth, determined through the number of slices between the focus planes of those ends; Δy is the in-plane distance between the ends determined through the number of pixels between them.

In the in-focus slice at the center of the wire, a line profile along the y-direction and through the point of highest intensity was created. The in-plane coordinate (y) was translated to the depth coordinate (z) by

$$z = y \cdot \tan \beta \qquad (2)$$

Thus, a profile along the z-direction was acquired and FWHM could be determined.

3.4 Artifact spread function

The artifact spread function (ASF) is a quantitative measurement of the out-of-plane blurring artifact in BT volume. An artifact from a real feature in the focus plane can be observed in other image planes. Ideally, the reconstruction algorithm should eliminate this artifact. In this work, the ASF was evaluated over a 3.1 mm diameter spherical mass of breast carcinoma simulating material and a 330 µm glass speck (Figure 5). The measurement setup (Figure 9), AEC settings and reconstruction options for this measurement were the same as for the measurement of the in-plane resolution described in section 3.3.1.

The ASF as a function of distance from the focus plane, z, is acquired as defined by Wu et al. (23):

$$ASF = \frac{\bar{\mu}_{artifact}(z) - \bar{\mu}_{bg}(z)}{\bar{\mu}_{feature}(z_0) - \bar{\mu}_{bg}(z_0)} \qquad (3)$$

where z is the distance to the focus plane, z_0 is $z = 0$, $\bar{\mu}_{artifact}$, $\bar{\mu}_{feature}$ and $\bar{\mu}_{bg}$ are the mean pixel value of the artifact, the feature and the background respectively.

To acquire $\bar{\mu}_{feature}$ and $\bar{\mu}_{artifact}$, a circular region-of-interest (ROI) was positioned in the feature (speck and spherical mass) and the artifact. The ROI size was selected to cover most of the area of the feature, i.e. 3.2 mm^2 for the sphere and 0.12 (GE)/0.15 mm^2 (Siemens) for the speck. The areas of the ROIs for Siemens and GE were not equal due to difference in pixel size. Also, as there was a slight translation of the feature caused by the reconstruction, the ROI was manually positioned. At the slices where the artifact was no longer visible, the ROI was placed at the same position as in the last slice where the artifact was visible.

To acquire $\bar{\mu}_{bg}$, another circular ROI was positioned in the homogenous background in every slice. The ROI area is the same as of the ROI placed inside the spherical mass for acquisition of $\bar{\mu}_{feature}$. For the background ROI, the in-plane position remained the same in every slice.

3.5   Optimization

3.5.1   Beam quality and dose evaluation in AEC settings

The AEC settings of both systems for varying breast thicknesses was evaluated as the first step to optimize the systems. For this evaluation, the CIRS phantom was used to acquire the values of the AEC settings (the default AEC option for GE and *OPDOSE* at normal dose level for Siemens). The range of phantom thicknesses was from 10 to 75 mm. The AGD values reported by the systems were compared to the dose limits set by the EUREF protocol for BT quality control (25).

3.5.2   Signal-difference-to-noise ratio

The signal-difference-to-noise ratio (SDNR) is a measurement of the detectability of a feature in the reconstruction plane and is defined as:

$$SDNR = \frac{\bar{\mu}_{feature} - \bar{\mu}_{background}}{\sigma_{background}} \qquad (4)$$

where $\bar{\mu}_{feature}$ and $\bar{\mu}_{background}$ are the mean pixel values of the feature and the background respectively, and $\sigma_{background}$ are the standard deviations of the pixel values of the feature and the background respectively.

For the SDNR measurement, both homogenous and heterogenous phantoms, CIRS models 020 and 021, were used. The measurement setup was similar to the one described in section 3.4.1 (Figure 9). The slab with imaging targets (Figure 5, Figure 7) was placed in the center of multiple homogenous or heterogenous slabs, adding up to a total thickness of 30, 45 and 70 mm. For the evaluation without the anatomical background, only homogenous slabs from CIRS phantom model 021 were used. On the contrary, both homogenous and heterogenous slabs were used in the evaluation with the anatomical background. The homogenous slabs were used to compensate for the lack of one 5mm thick heterogenous slab for the 45 mm setup and one 10 mm thick slab for the 70 mm set up. The added homogenous slabs were positioned as a base. As

each heterogenous slab has a unique pattern, the arrangement of the heterogenous slabs was maintained for all measurements.

The images were acquired with varying tube loading values and subsequently reconstructed. For the Siemens system, two different reconstruction algorithms were used to reconstruct the tomosynthesis volume for evaluation, one was the clinically used *TOMO_STANDARD* and the other was Siemens newly developed algorithm *EMPIRE*. For the GE system, the reconstruction algorithm *ASiR1* was used.

For all images, the SDNR was evaluated over a 6.3 mm diameter spherical mass of breast carcinoma simulating material and 330/400 µm glass speck (Figure 5, Figure 7). $\bar{\mu}_{feature}$ was acquired using a circular ROI positioned in the center of the sphere/speck, covering most of the area of the feature. To acquire $\bar{\mu}_{background}$ and $\sigma_{background}$, different methods were used for the homogenous and heterogenous phantom images. For the homogenous phantom images, only one circular ROI was positioned in the artifact-free background. For the heterogenous phantom, because of the anatomical noise, the values of $\bar{\mu}_{background}$ and $\sigma_{background}$ from one single ROI changed drastically depending on the ROI position. Thus, multiple half-overlapping ROIs positioned in a doughnut-like shape, were used to acquire average values of $\bar{\mu}_{background}$ and $\sigma_{background}$ (Figure 10). The circular outline of the feature was used as the guideline for positioning of the overlapping ROI. The number of ROIs and the ROI area for evaluation of different features in both phantoms are presented in Table 2.
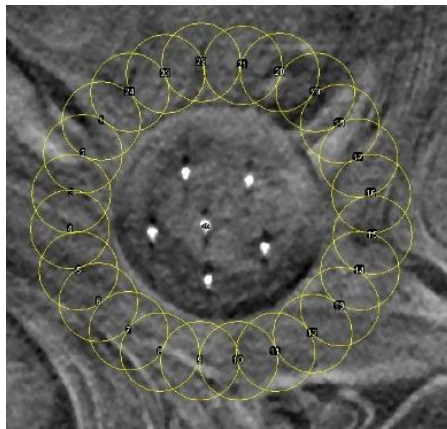

Figure 10: Half-overlapping background ROI

for evaluation of the heterogenous phantom images.

Table 2: ROI set-up for evaluation of different features in both CIRS phantoms.

Feature	GE		Siemens	
	Feature ROI	Background ROI	Feature ROI	Background ROI
6.3 mm mass in CIRS 021	1 x 17.4 mm^2	1 x 17.4 mm^2	1 x 17.2 mm^2	1 x 17.2 mm^2
330 µm speck in CIRS 021	1 x 0.03 mm^2	1 x 17.4 mm^2	1 x 0.04 mm^2	1 x 17.2 mm^2
6.3 mm mass in CIRS 020	1 x 17.4 mm^2	22 x 17.4 mm^2	1 x 17.2 mm^2	22 x 17.2 mm^2
400 µm speck in CIRS 020	1 x 0,09 mm^2	24 x 17.4 mm^2	1 x 0.09 mm^2	24 x 17.2 mm^2

4 Results & discussion

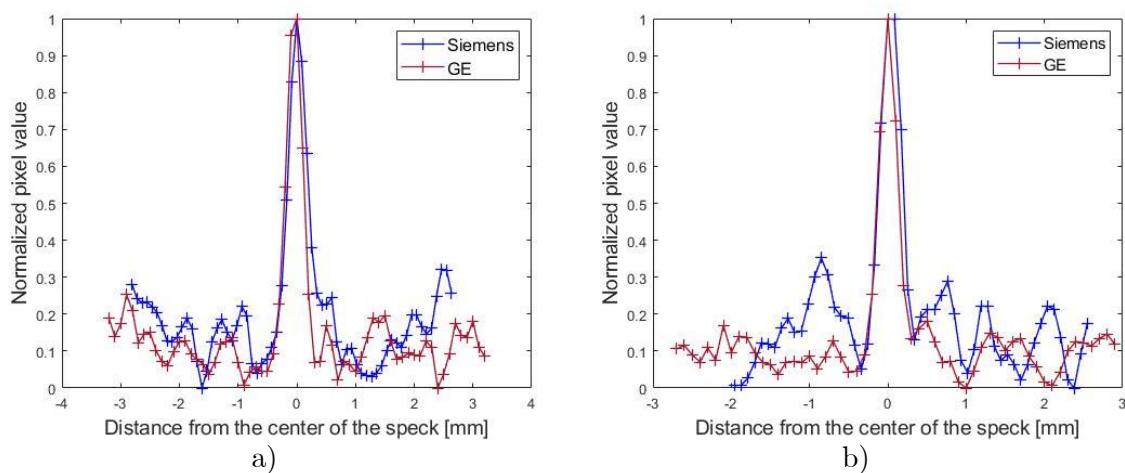## 4.1 Spatial resolution

4.1.1 In-plane resolution

a) b)

Figure 11: The in-plane point spread function (PSF) of 330 µm glass speck in a) x-direction (parallel to the tube travel direction) b) y-direction (orthogonal to the tube travel direction)

Table 3: FWHM values of the PSF in x- and y-direction of both systems.

Direction	FWHM [μm]	
	GE	Siemens
x-direction	330	380
y-direction	290	340

In Figure 11, the in-plane point spread functions (PSF) in x and y-directions acquired for the 330 μm glass speck are shown. The pixel values of both systems were normalized to the range [0-1]. The FWHM of the PSF are presented in Table 3. We observe in a) a larger fluctuation of background pixel values for the Siemens system. The higher noise is expected of FBP as discussed in section 2.3.5 (23). As the pixel values were normalized without thresholding the background signals, there is an uncertainty in the measured FWHM, if a ringing artifact is present, the method will give an uncertainty to the FWHM value.

In both directions, the GE system has a smaller FWHM compared to the Siemens system. The difference is however not significant and will not be differentiated in the clinical images, because it is approximately half of the pixel size of the systems which are 100 μm and 85 μm (Table 1). The in-plane resolution is affected by the detector, the acquisition geometry, the reconstruction algorithms, the focal spot size and motion. Regarding the detector, GE with indirect conversion detector with larger pixel size should have wider PSF, which is not the case here. However, the result agrees partly with the comparison between IR and FBP by Zhou et al. (18) discussed in section 2.3.5. In the study, IR overall shows better performance regarding in-plane resolution, which is the case here. The authors also conclude that FBP can provide the same performance when increasing the number of projections and the total angular range, i.e. 21 views in ± 30 which is close to the construction of the investigated Siemens system. This disagreement may be due to the difference in the IR technique and FBP filter. Also, moving the focal spot during exposure gives a blur and can explain the larger FWHM of the Siemens system.

Another study (21) suggests that the resolution in x-direction is better for narrow angular range, which concurs with our result.

4.1.2 Depth resolution

The depth PSF of both investigated systems are presented in Figure 12. The pixel values were normalized to the range [0-1]. The FWHM for both systems are shown in Table 4. Once again, there was no background thresholding before the normalization, causing

an uncertainty in the FWHM values. Because the Siemens system has a larger fluctuation in the background signals, the measured FWHM for the system also has larger uncertainty compared to that of the GE system. Additionally, the signal of the Siemens system decreases and then increases again at further distance from the center plane, indicating a ringing artifact. However, these factors are not the only contributing factors to the large difference between the PSFs of the systems as observed in Figure 12.

As discussed in section 2.3.4., the Siemens system with wider angular range and larger number of projection views should have better depth resolution compared to the GE system. However, our result may be explained by the counter effect of the reconstruction algorithm, as IR is more effective in noise and artifact reduction compared to FBP.
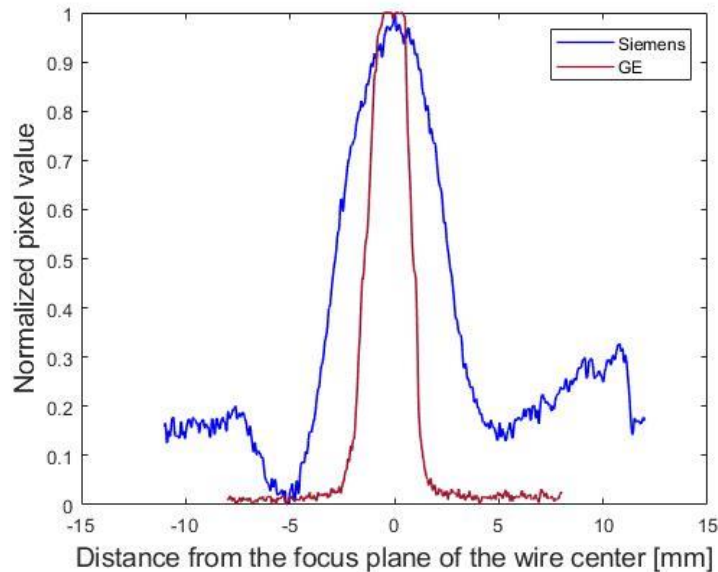

Figure 12: Depth resolution evaluated over the 150 µm diameter wire.

Table 4: FWHM values of the PSF in z-direction of both systems.

FWHM [mm]	
GE	Siemens
2.3	5.5

4.2   Artifact spread function

Figure 13 shows the ASF evaluated over the 3.1 mm diameter carcinoma sphere and the 330 µm glass speck. It is remarkable that in both cases, some ASF values are

negative. This means that the mean pixel value in the background, $\bar{\mu}_{bg}(z)$, is higher than the mean pixel value in the artifact, $\bar{\mu}_{artifact}(z)$, (see Equation 3) in some planes, indicating an uncertainty due to the fluctuation of the signal. The uncertainty is reduced when averaging for large ROI, thus there are fewer negative values in the evaluation over the 3.1 mm carcinoma sphere than the 330 µm glass speck.

The FWHM of the ASF are presented in Table 5. For the carcinoma, the ASF of the Siemens system is narrower compared to the ASF of the GE system, while for the glass speck, the opposite applies. As discussed in section 2.3.4 and 2.3.5, the ASF is partly affected by the total angular range, the number of projection views, and the reconstruction algorithm. In the matter of acquisition geometry, Siemens with larger total angular range and higher number of projection views should result in more confined ASF. On the other hand, regarding reconstruction algorithm, the GE system with IR should perform better. In this case where the ASF for carcinoma sphere and the glass speck differ, it may be due to the IR being more effective in reducing artifact of high contrast objects and the influence of the reconstruction algorithm becomes more dominant than the acquisition geometry.

It is difficult to decide whether the difference in ASF between the systems is significant. Even though there is a difference between the ASF curves, it is not certain that the difference is visible in the clinical images, thus a qualitative evaluation from a radiologist is needed to complete this investigation.
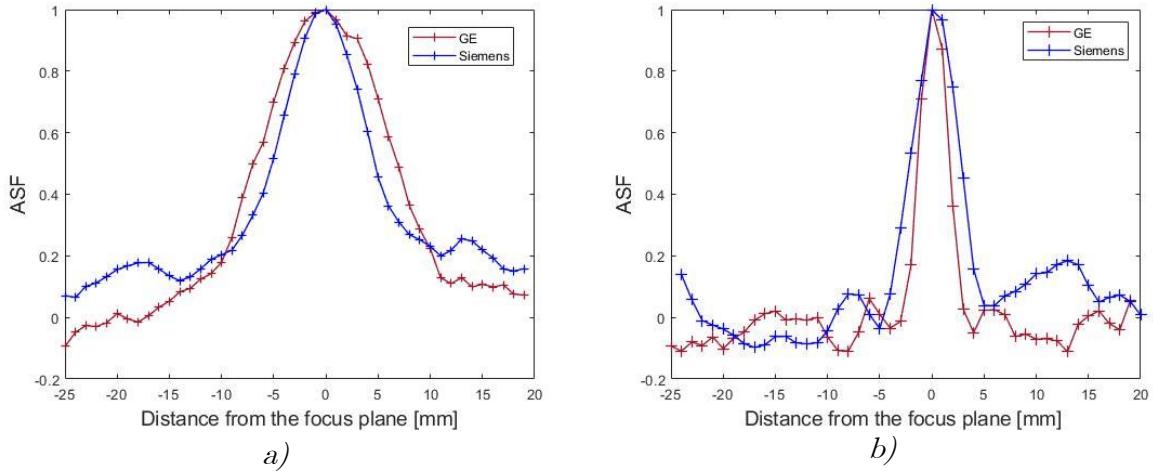

Figure 13: Artifact spread function (ASF) evaluated using 45 mm homogenous breast phantom with a) 3.1 mm diameter carcinoma sphere b) 330 µm glass speck

Table 5: FWHM values of the ASF for 3.1 mm diameter carcinoma sphere and 330 µm glass

Feature	FWHM [mm]	
	GE	Siemens
3.1 mm mass	13.9	9.8
330 µm speck	3.1	5.0

The ASF of a feature significantly smaller than the reconstruction thickness is approximately equal to the depth resolution. This also concurs with our result regarding the ASF of the 330 µm glass speck (Table 5) and the depth resolution (Table 4).

4.3   Optimization

4.3.1   Beam quality and dose evaluation in AEC settings

The AEC settings presented in Table 6 were used to perform the exposures of the homogenous CIRS phantom at different breast thicknesses. The X-ray spectra produced at each AEC setting were simulated and presented in the Appendix.

Table 6: Exposure parameters with AEC settings and the AGD reported by the systems for different breast thickness.

Breast thickness [mm]	Tube voltage [kV]		Anode/filter combination		Tube loading [mAs]		AGD [mGy]	
	GE	Siemens	GE	Siemens	GE	Siemens	GE	Siemens
10	26	25	Mo/Mo	W/Rh	18.1	55.0	0.70	0.90
20	26	25	Mo/Mo	W/Rh	18.1	64.0	0.70	0.91
30	26	26	Mo/Mo	W/Rh	38.6	89.5	0.76	1.17
40	34	27	Rh/Ag	W/Rh	23.4	125.0	0.99	1.50
50	34	28	Rh/Ag	W/Rh	32.2	175.5	1.15	1.97
60	34	29	Rh/Ag	W/Rh	50.4	243.0	1.57	2.61
65	34	30	Rh/Ag	W/Rh	62.6	262.5	1.88	2.92
75	34	31	Rh/Ag	W/Rh	86.2	343.8	2.88	3.75

The GE system uses only two beam qualities (26 kV, Mo/Mo and 34 kV, Rh/Ag) for breast thickness under 40 mm and at or over 40 mm, respectively. The Siemens system on the contrary, adjusts the tube voltage continuously depending on the breast thickness, using harder beams for larger breast thicknesses. In the smaller breast thickness range (10 - 30mm), the GE system uses much lower mean photon energy compared to the Siemens system. In the larger breast thickness range (40 – 70mm), the Siemens system uses lower mean photon energy compared to the GE system, although the energy difference decreases with increasing breast thickness (see Appendix).

In Figure 14, the AGD values from AEC settings for different breast thickness of both the GE and Siemens systems are presented with EUREF dose limits for BT (25). Both systems are below the EUREF dose limits, although the GE system consistently uses a lower AGD compared to the Siemens system for all breast thickness.
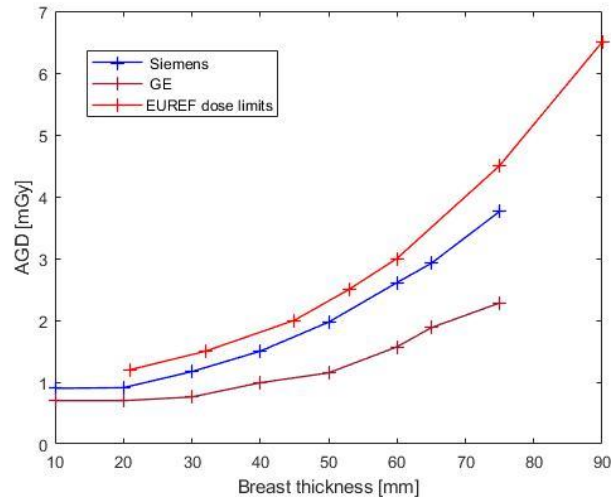

Figure 14: Average glandular dose of clinical AEC settings in GE and Siemens system compared to EUREF dose limits for breast tomosynthesis.

4.3.2 Signal-difference-to-noise ratio

Figure 15 – 17 shows the SDNR as a function of AGD of different anatomical features and backgrounds in 30 mm, 45 mm and 70 mm phantom thickness. From the previous section, we note that at AEC setting, the GE system uses a lower AGD than the Siemens system for all breast thickness. Thus, it is of interest to evaluate whether the SDNR of the systems are comparable. As shown in Figure 15 – 17, the GE system has comparable or higher SDNR than the Siemens system with *TOMO_STANDARD* at AEC setting for all the feature and background setups even though the AGD is lower

for the GE system. However, the newly developed reconstruction algorithm *EMPIRE* results in SDNR values that are significantly higher than *TOMO_STANDARD* in all cases, except for the evaluation of the glass specks in 30 mm swirl phantom (Figure 15d). In most cases, Siemens *EMPIRE* gives SDNR values that are comparable or even higher compared to the GE system.
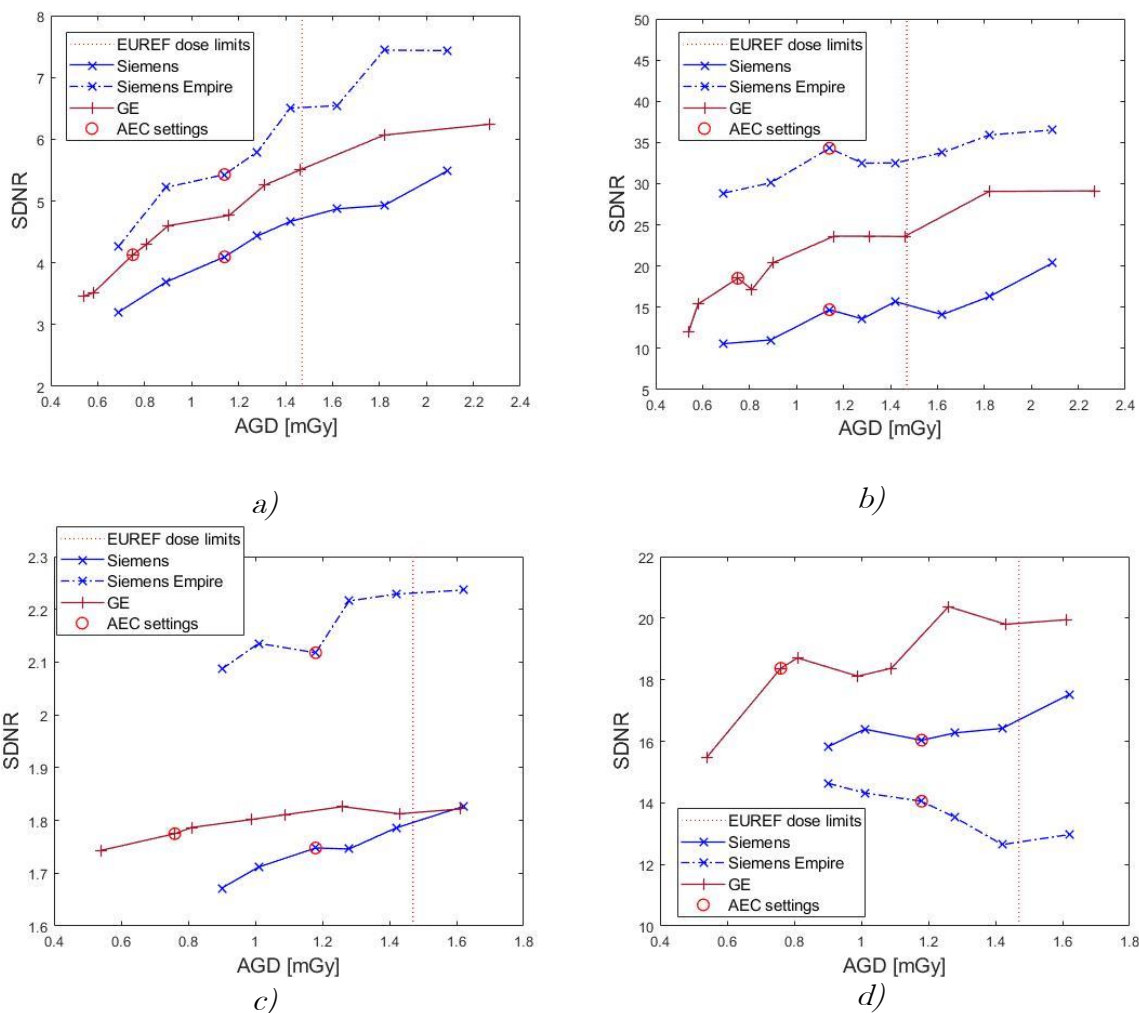

Figure 15: SDNR as a function of AGD for 30 mm breast thickness, evaluated over a) 6.3 mm diameter carcinoma sphere in homogenous phantom (CIRS 021) b) 330 µm diameter glass speck in homogenous phantom (CIRS 021) c) 6.3 mm diameter carcinoma sphere in heterogenous phantom (CIRS 020) d) 330 µm diameter glass speck in heterogenous phantom (CIRS 020).

It is notable that Siemens *EMPIRE* gives decreasing SDNR at higher AGD for the glass speck in swirl phantoms (Figure 15 – 17 d). Because of the occurrence in all three breast thicknesses, it should not be a coincidence. It is unexpected because the SDNR should increase with absorbed dose, as discussed in section 2.3.1. It is also remarkable that the

behavior is not observed in the cases of the glass specks in homogenous phantom (Figure 15 – 17 c). The reason behind this is unknown, but it may be related to the fact that *EMPIRE* uses a statistical model trained on patient data and thus behaves differently for homogenous backgrounds. When evaluating the BT volumes, we also observe that the *EMPIRE* glass specks are more blurred out than the *TOMO_STANDARD*. It may be the intention of the manufacturer to make the speck appear larger to compensate for the lower contrast, but further investigation is needed. It is also notable that all the SDNR values for the glass speck are greater than 10, so an increasing or decreasing tendency may not affect the visibility of the speck.
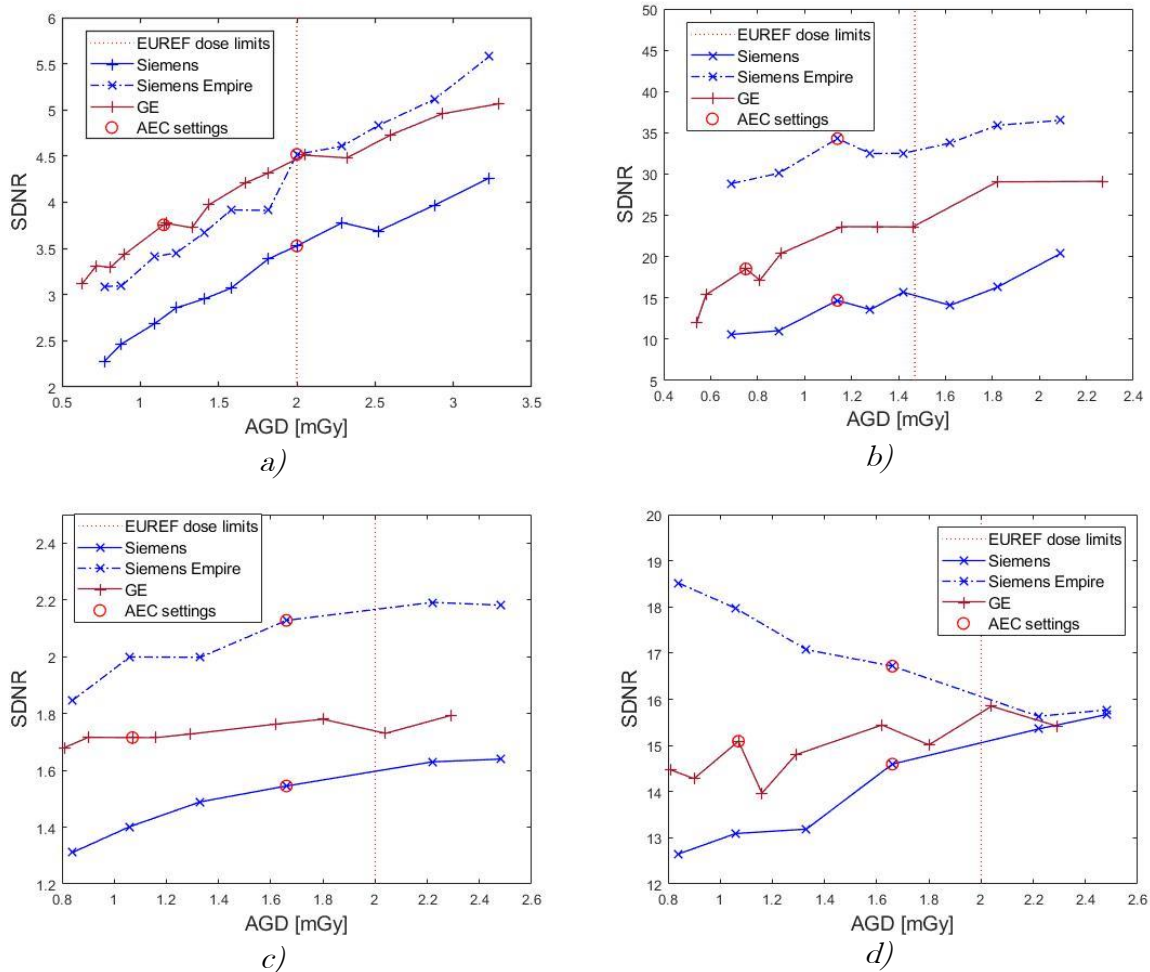

Figure 16: SDNR as a function of AGD for 45 mm breast thickness, evaluated over a) 6.3 mm diameter carcinoma sphere in homogenous phantom (CIRS 021) b) 330 μm diameter glass speck in homogenous phantom (CIRS 021) c) 6.3 mm diameter carcinoma sphere in heterogenous phantom (CIRS 020) d) 330 μm diameter glass speck in heterogenous phantom (CIRS 020).

Overall, the SDNR values of the glass specks (Figure 15-17 b,d) are higher than of the carcinoma spheres (Figure 15-17 a,c). This is expected as the glass specks has higher

density. Also, the SDNR curves measured over the glass specks are more irregular than measured over the spheres. It is reasonable since the ROI area of the speck is much smaller than of the spheres, causing the mean pixel value to be more unstable. Considering the effect of the anatomical noise, we observe generally lower SDNR values with anatomical noise (Figure 15-17 c,d) than without (Figure 15-17 a,b) for all features. With the swirl phantom, the SDNR gain with higher AGD is small compared to the SDNR gain with the homogenous phantom. Based only on the results from the homogenous phantom, we can suggest that the image quality can be improved by increasing the absorbed dose. However, the results with the swirl phantom, that is more similar to real breasts, suggest that it is not beneficial to increase the absorbed dose for a small gain in SDNR.
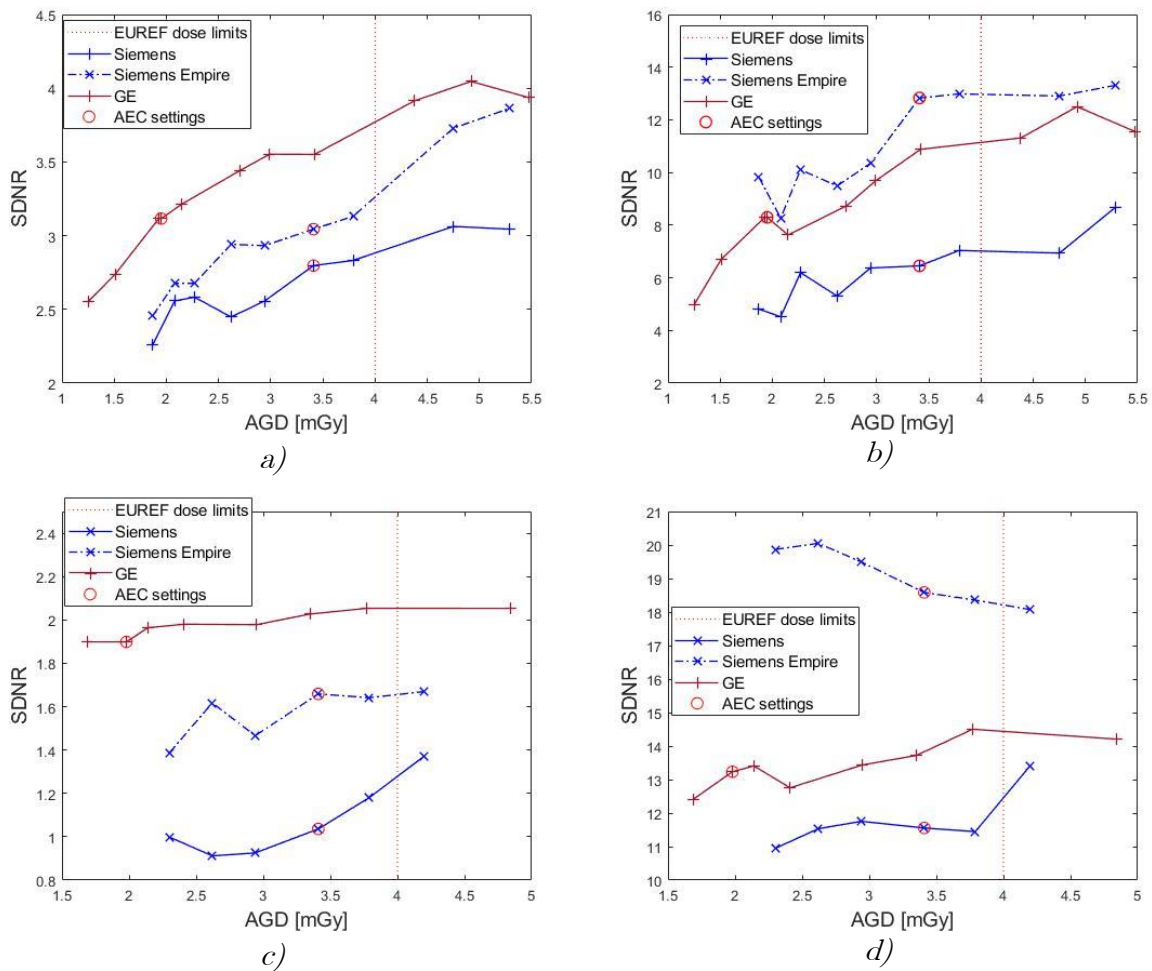

Figure 17: SDNR as a function of AGD for 70 mm breast thickness, evaluated over a) 6.3 mm diameter carcinoma sphere in homogenous phantom (CIRS 021) b) 330 µm diameter glass speck in homogenous phantom (CIRS 021) c) 6.3 mm diameter carcinoma sphere in heterogenous phantom (CIRS 020) d) 330 µm diameter glass speck in heterogenous phantom (CIRS 020).

26

There are some factors which contribute to the uncertainties of the results in this section. One main factor causing the irregularity of the SDNR curves was the placement of the background ROI. It is especially important in the evaluation of the homogenous phantom because only one background ROI was used (Table 2). Due to the reconstruction, the edge of the image appears faded compared to the center (Figure 18), thus shifting the values of $\bar{\mu}_{background}$ and $\sigma_{background}$ depending on the ROI position. Due to that the BT volumes have different dimensions and the placement of the phantom is not exactly the same after every measurement setup, the ROIs were merely manually placed at roughly the same position in the image. This problem causes difficulty in replicating the results using the same method. For a more stable result, multiple SDNR values of different backgrounds need to be calculated and averaged. In the case of the heterogenous phantom, a group of overlapping background ROI were used to reduce the impact of anatomical noise. However, a slight change in the position of the whole ROI group still affects the values of $\bar{\mu}_{background}$ and $\sigma_{background}$ drastically. The uncertainty is difficult to estimate and is therefore excluded from our results.
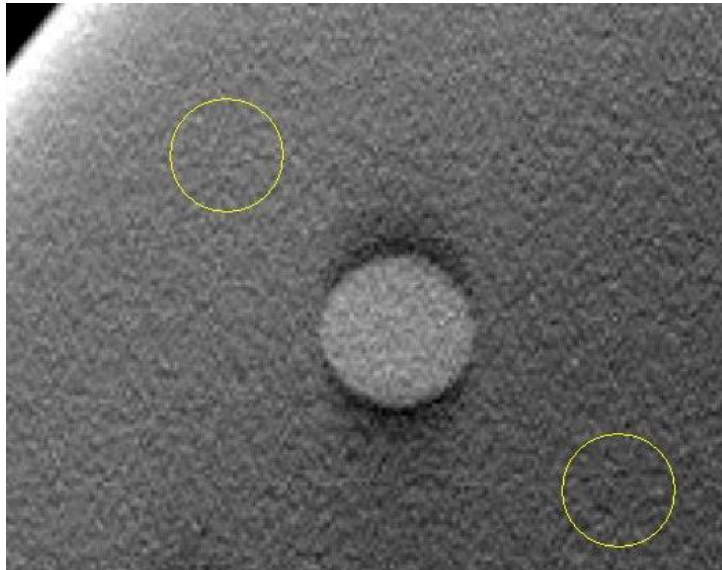

Figure 18: Different ROI placement.

5   Conclusion

This study did not demonstrate a clear advantage of any system. The GE system and the Siemens system shows better performance in different aspects. Also, consideration must be given to uncertainties in the measured data that originate from the non-robust method of quantification on reconstructed and processed images.

Regarding the optimization, according to our results, a dose increase does not result in a significant SDNR gain. However, it might enhance the other image quality aspects that were not investigated in this study. Also, Siemens *EMPIRE* shows promising result considering the improvement of SDNR.

Due to the time limit, this study did not include a qualitative evaluation by radiologists. Such an evaluation should be performed in order to complement the current study to give a complete overview for a concrete comparison and further optimization.

References

1.   Socialstyrelse. Cancer i siffror. Socialstyrelse; 2018.
2.   Socialstyrelse. Screening för bröstcancer - rekommendation och bedömningsunderlag. Socialstyrelse; 2014.
3.   Vedantham S, Karellas A, Vijayaraghavan GR, Kopans DB. Digital Breast Tomosynthesis: State of the Art. 2015;277(3):663-84.
4.   Niklason LT, Christian BT, Niklason LE, Kopans DB, Castleberry DE, Opsahl-Ong BH, et al. Digital tomosynthesis in breast imaging. Radiology. 1997;205(2):399-406.
5.   Ciatto S, Houssami N, Bernardi D, Caumo F, Pellegrini M, Brunelli S, et al. Integration of 3D digital mammography with tomosynthesis for population breast-cancer screening (STORM): a prospective comparison study. The Lancet Oncology. 2013;14(7):583-9.
6.   Zackrisson S, Lang K, Rosso A, Johnson K, Dustler M, Fornvik D, et al. One-view breast tomosynthesis versus two-view mammography in the Malmo Breast Tomosynthesis Screening Trial (MBTST): a prospective, population-based, diagnostic accuracy study. Lancet Oncol. 2018;19(11):1493-503.
7.   Vyborny CJ, Schmidt RA. Mammography as a radiographic examination: an overview. RadioGraphics. 1989;9(4):723-64.
8.   Stanton L, Lightfoot DA, James J. Boyle J, Cullinan JE. Physical Aspects of Breast Radiography. 1963;81(1):1-16.
9.   Gershon-Cohen J, Hermel MB, Birsner JW. Advances in mammographic technique. Am J Roentgenol Radium Ther Nucl Med. 1970;108(2):424-7.
10.   Haus AG. Historical Technical Developments in Mammography. 2002;1(2):119-26.
11.   Maidment ADA, Fahrig R, Yaffe MJ. Dynamic range requirements in digital mammography. 1993;20(6):1621-33.
12.   Bick U, Diekmann F. Digital Mammography: Springer Berlin Heidelberg.
13.   Dobbins JT, 3rd, Godfrey DJ. Digital x-ray tomosynthesis: current state of the art and clinical potential. Phys Med Biol. 2003;48(19):R65-106.
14.   Bankman IN. Handbook of medical imaging: processing and analysis. San Diego, CA: Academic Press; 2000.
15.   Samei E, Flynn MJ. An experimental comparison of detector performance for direct and indirect digital radiography systems. 2003;30(4):608-22.
16.   Maidment A, Albert M, Thunberg S, Adelow L, Blom O, Egerstrom J, et al. Evaluation of a photon-counting breast tomosynthesis imaging system: SPIE; 2005.
17.   Maidment ADA, Ullberg C, Lindman K, Adelöw L, Egerström J, Eklund M, et al. Evaluation of a photon-counting breast tomosynthesis imaging system: SPIE; 2006.
18.   Zhou J, Zhao B, Zhao W. A computer simulation platform for the optimization of a breast tomosynthesis system. 2007;34(3):1098-109.
19.   Bissonnette M, Hansroul M, Masson E, Savard S, Cadieux S, Warmoes P, et al. Digital breast tomosynthesis using an amorphous selenium flat panel detector: SPIE; 2005.
20.   Hu Y-H, Zhao B, Zhao W. Image artifacts in digital breast tomosynthesis: Investigation of the effects of system geometry and reconstruction parameters using a linear system approach. 2008;35(12):5242-52.

21.   Lu Y, Chan H-P, Wei J, Goodsitt M, Carson PL, Hadjiiski L, et al. Image quality of microcalcifications in digital breast tomosynthesis: effects of projection-view distributions. Medical physics. 2011;38(10):5703-12.

22.   Van de Sompel D, Brady SM, Boone J. Task-based performance analysis of FBP, SART and ML for digital breast tomosynthesis using signal CNR and Channelised Hotelling Observers. Medical Image Analysis. 2011;15(1):53-70.

23.   Wu T, Moore RH, Rafferty EA, Kopans DB. A comparison of reconstruction algorithms for breast tomosynthesis. 2004;31(9):2636-47.

24.   Abdurahman S, Jerebko A, Mertelmeier T, Lasser T, Navab N. 2012. Out-of-plane artifact reduction in tomosynthesis based on regression modeling and outlier detection: Breast Imaging. IWDM 2012.

25.   Engen REv, Bosmans H, Bouwman RW, Dance DR, Heid P, Lazzari B, et al. 2018. Protocol for the Quality Control of the Physical and Technical Aspects of Digital Breast Tomosynthesis Systems, v1.03. Europan Reference Organisation for Quality Assured Breast Screening and Diagnostic Services, EUREF.

26.   Simulation of X-ray Spectra [Internet]. Simulation of X-ray Spectra - Siemens OEM X-Ray Components. Siemens Healthineers; [cited 2019May31]. Available from: https://www.oem-products.siemens-healthineers.com/x-ray-spectra-simulation

Appendix

The beam qualities of GE Senographe Pristina and Siemens Mammomat Inspiration are simulated using an online tool of Siemens Healthcare GmbH (26). The parameters applied for the simulation were acquired from Table 1 and Table 6.
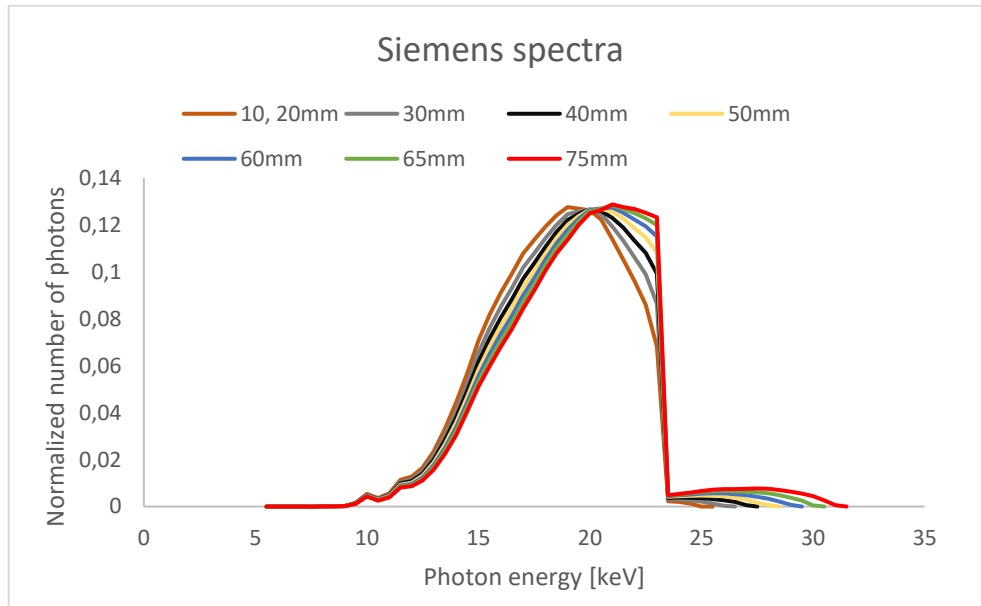

Figure 19: The simulated X-ray spectra of Siemens, produced using AEC settings for different breast thickness.
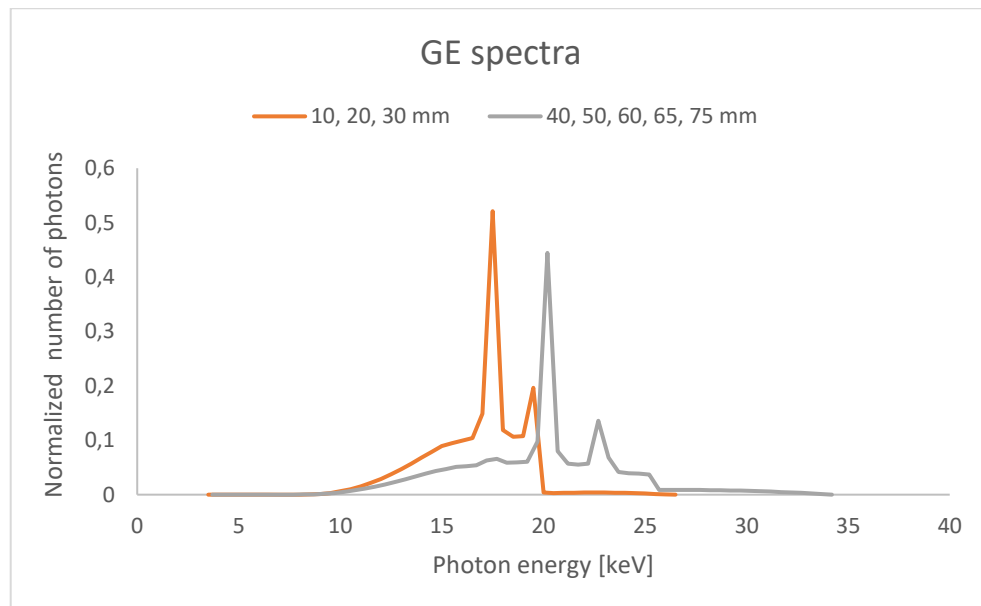

Figure 20: The simulated X-ray spectra of GE, produced using AEC settings for different breast thickness.

Table 7: Mean photon energy of Siemens and GE X-ray spectrum produced using AEC settings for different breast thickness.

Breast thickness [mm]	Mean photon energy [keV]	
	GE	Siemens
10	16.234	18.434
20	16.234	18.434
30	16.234	18.645
40	19.845	18.821
50	19.845	18.973
60	19.845	19.122
65	19.845	19.274
75	19.845	19.443